Supporting Information for

# Reaction Mechanism for α-$MnO_2$ Cathode in Aqueous Zn Ion Batteries Revisited: Elucidating Irreversible Transformation of α-$MnO_2$ to Zn-vernadite

Shuangshuang Cui,[ab] Dan Zhang*[ab], Guoxu Zhang, [ab] and Yang Gan*[ab]

a. School of Chemistry and Chemical Engineering, Harbin Institute of Technology, Harbin 150001, People's Republic of China. E-mail: ygan@hit.edu.cn, zhangd@hit.edu.cn
b. MIIT Key Laboratory of Critical Materials Technology for New Energy Conversion and Storage, School of Chemistry and Chemical Engineering, Harbin Institute of Technology, Harbin 150001, People's Republic of China

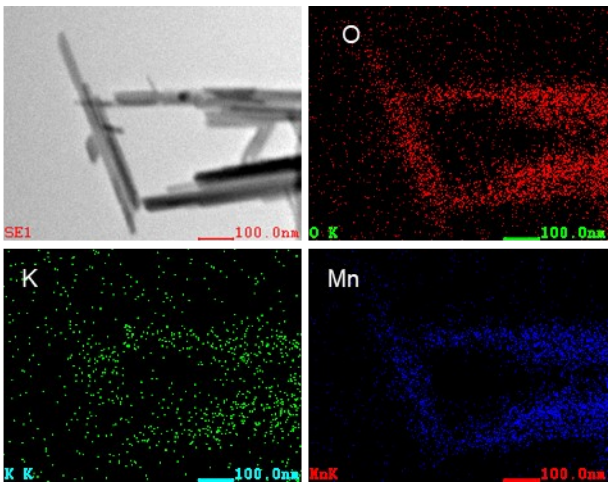


Fig. S1 TEM image and the corresponding EDS elemental mapping images of α-$MnO_2$ nanorods.

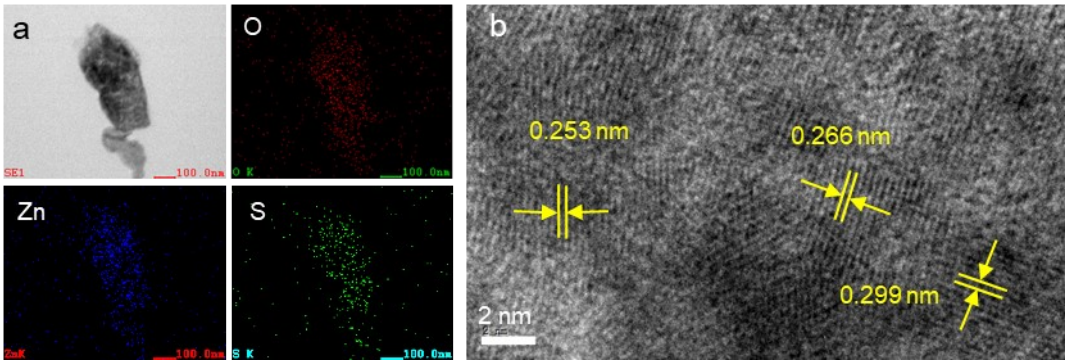


Fig. S2 TEM EDS elemental mappings and HRTEM image of ZHS paticles. (a) TEM image and the corresponding EDS elemental mapping images. (b) HRTEM image. The lattice spacing of 0.266 nm, 0.299 nm and 0.253 nm correspond to (121), $(2\bar{1}3)$ and $(2\bar{3}2)$ planes of ZHS.

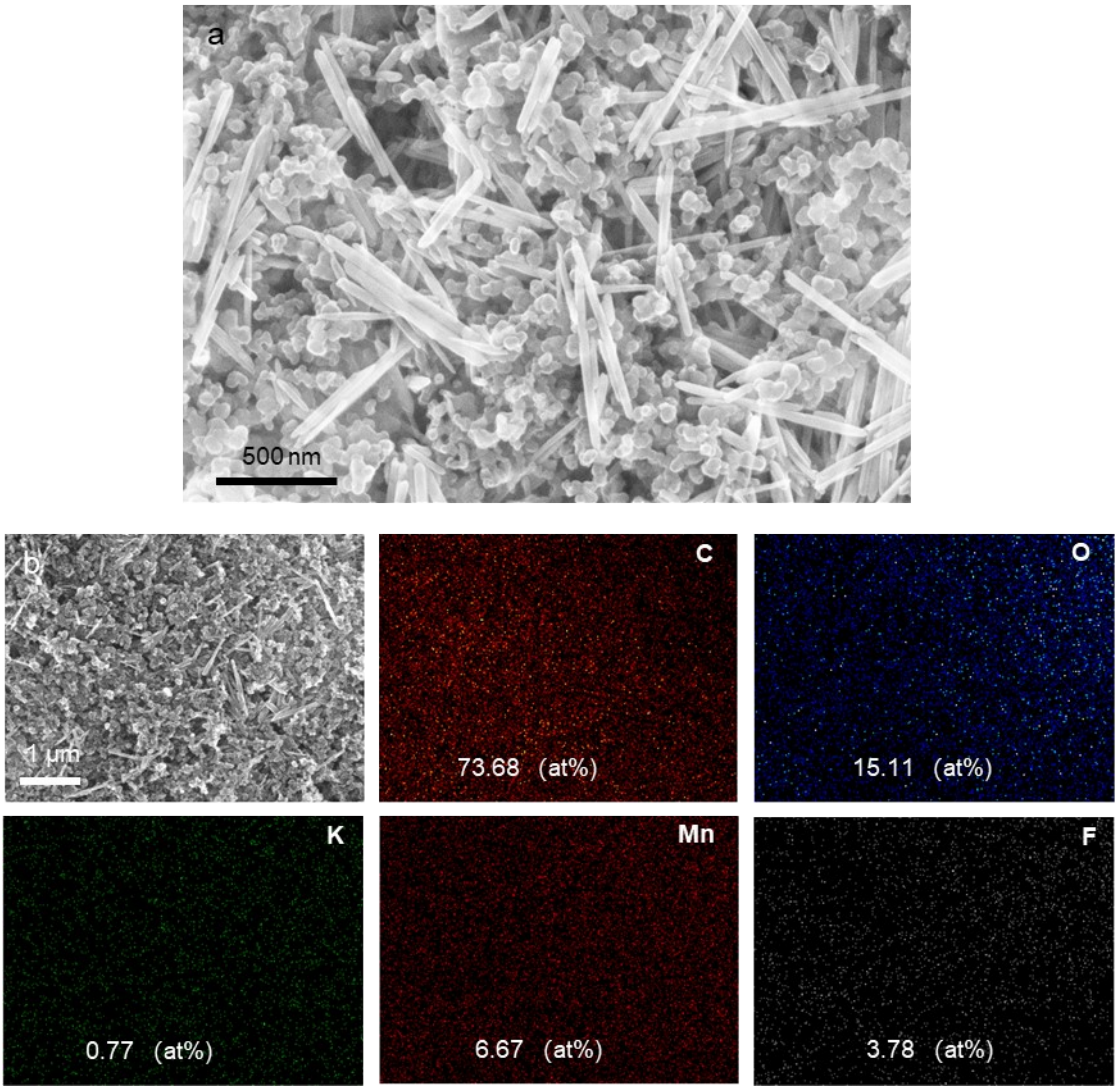


Fig. S3 SEM image and the corresponding EDS elemental mapping images of discharged α-$MnO_2$ electrode after acetic acid treatment. (a) SEM image. (b) EDS elemental mapping images.

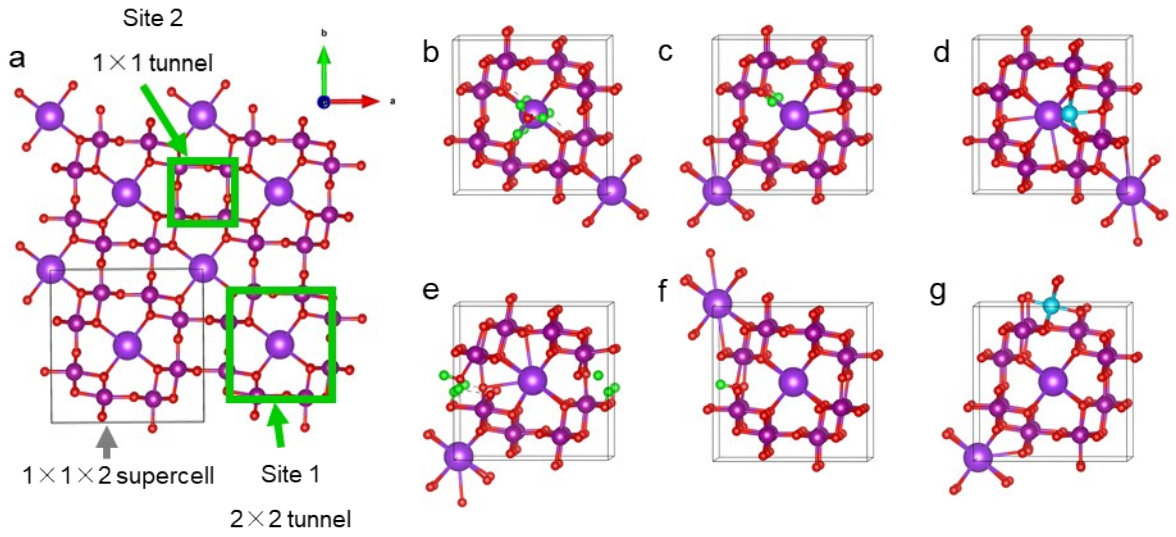


Fig. S4 Structure model of α-$MnO_2$, and optimized structure of $H_3O^+$, $Zn^{2+}$ and $H^+$ intercalated α-$MnO_2$ via DFT calculations. (a) Structure model of α-$MnO_2$. Optimized structure of various cations intercalated into 2×2 tunnels of α-$MnO_2$: (b) $H_3O^+$, (c) $Zn^{2+}$ and (d) $H^+$. Optimized structure of of various cations intercalated into 1×1 tunnels of α-$MnO_2$: (e) $H_3O^+$, (f) $Zn^{2+}$ and (g) $H^+$.

The formation energy for intercalation of $H^+$, $H_3O^+$ and $Zn^{2+}$ into 2×2 tunnels (site 1) and 1×1 tunnels (site 2) in α-$MnO_2$ containing $K^+$ were calculated (the number of $K^+$ in the structure model of α-$MnO_2$ was set based on the measured $K^+$ content in α-$MnO_2$ samples prepared by hydrothermal method). Only the formation energy of desolvated $Zn^{2+}$ intercalated α-$MnO_2$ was calculated because the size of $[Zn(H_2O)_6]^{2+}$ is too large[1, 2] to intercalate into the 2×2 tunnels and the smaller sized 1×1 tunnels of α-$MnO_2$.

Details of calculation of the formation energy of $Zn^{2+}$, $H^+$ or $H_3O^+$ intercalated into α-$MnO_2$ are as follows. The first-principles DFT calculations were performed with VASP using the PAW method. The exchange-functional was treated using the generalized gradient approximation of PBE functional. The energy cutoff for the plane wave basis expansion was set to 450 eV and the force on each atom less than 0.02 eV/Å was set for convergence criterion of geometry relaxation. The 1×1×2 supercell of α-$MnO_2$ with two embedded K atoms were adopted for simulations. Brillouin-zone integration was sampled by 3×3×5 k-point sampling. The self-consistent calculations apply a convergence energy threshold of $10^{-5}$ eV. The DFT-D3 method was employed to consider the van der Waals interaction. The formation energy of $Zn^{2+}$, $H^+$ or $H_3O^+$ intercalated into α-$MnO_2$ was calculated according to the equation:

$$E_f = E_{tot} - E_{ions} - E_{MnO_2},$$

where $E_{tot}$ is the total energy of the $Zn^{2+}$, $H^+$ or $H_3O^+$ intercalated into α-$MnO_2$, $E_{ions}$ is the energy of the isolated $H_3O^+$, $H^+$, or $Zn^{2+}$, $E_{MnO_2}$is the energy of the α-$MnO_2$ substrate.

Table S1. Formation energy for intercalation of $H^+$, $H_3O^+$ and $Zn^{2+}$ in α-$MnO_2$

| Cations | Intercalation sites[#] | $E_{tot}$ (eV) | $E_{MnO_2}$(eV) | $E_{ions}$ (eV) | $E_f$(eV) |
|---|---|---|---|---|---|
| $H^+$ | 1 | -402.64 | -399.03 | -6.77 | -0.22 |
| | 2 | -402.44 | -399.03 | -6.77 | -0.022 |
| $H_3O^+$ | 1 | -417.93 | -399.03 | -14.92 | -3.98 |
| | 2 | -411.50 | -399.03 | -14.92 | 2.45 |
| $Zn^{2+}$ | 1 | -400.23 | -399.03 | -0.0079 | -1.18 |
| | 2 | -399.05 | -399.03 | -0.0079 | -0.0048 |

[#] The intercalation sites were shown in Fig. S4a.

Table S2. Lattice parameters of α-$MnO_2$ before and after $H_3O^+$ intercalation: comparison of DFT calculation and *operando* XRD[#] results.

| DFT calculation or *operando* XRD results | Intercalation states of α-$MnO_2$ | lattice parameters (Å)[#] | | | |
|---|---|---|---|---|---|
| | | *a* | *b* | *c* | unit cell volume |
| DFT calculation | Before $H_3O^+$ intercalation | 9.7646 | 9.7566 | 2.8467 | 271.2031 |
| | After $H_3O^+$ intercalation | 9.7936 | 9.7885 | 2.8408 | 272.3323 |
| *Operando* XRD | Before the 1st discharge | 9.8506 | 9.8506 | 2.8621 | 277.7219 |
| | After the 1st discharge | 9.9319 | 9.9319 | 2.8553 | 281.6543 |

[#] The change of lattice parameters of α-$MnO_2$ during the 1st discharge was obtained from *operando* XRD patterns with the equation:

$$\frac{1}{d^2} = \frac{h^2 + k^2}{a^2} + \frac{l^2}{c^2}.$$

Because the peaks of (200), (211) and (301) planes of α-$MnO_2$ did not overlap with the peaks of ZHS, the lattice spacings (*d*) of these planes were calculated with Bragg equation for the corresponding peak positions in *operando* XRD patterns.

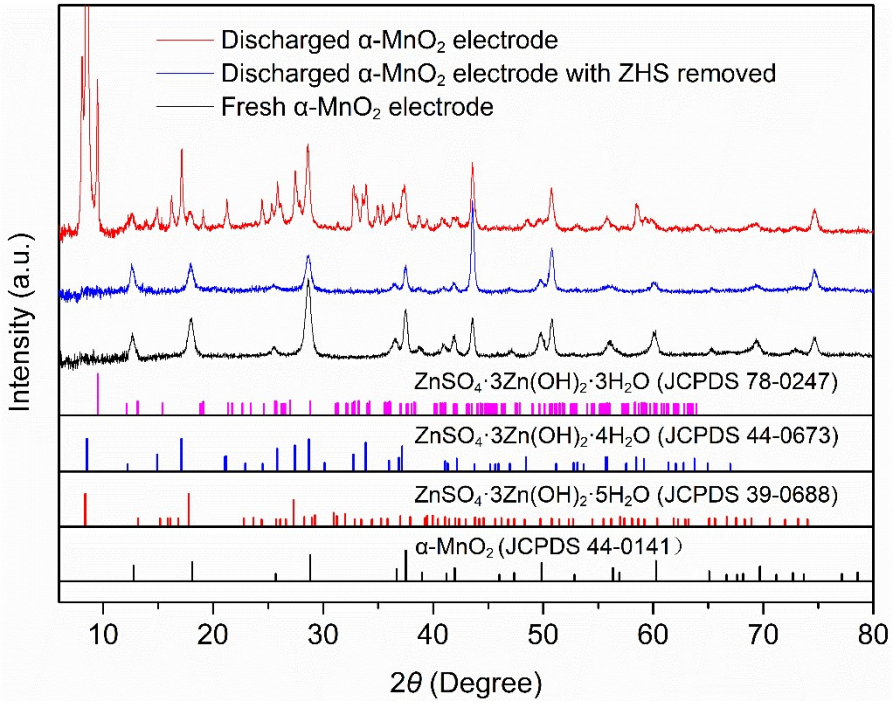


Fig. S5 *Ex situ* XRD patterns of fresh α-$MnO_2$ electrode, α-$MnO_2$ electrode after the 1st discharge, and α-$MnO_2$ electrode after the 1st discharge with ZHS removed.

The decreased intensity of α-$MnO_2$ peaks after the 1st discharge can be attributed to either formation of ZHS covering the electrode or loss in amount of α-$MnO_2$. Then, ZHS was removed from the discharged electrode by acetic acid treatment and characterized using *ex situ* XRD. The peaks of α-$MnO_2$ reduced significantly in intensity after removal of ZHS compared with that before discharge, revealing the loss in amount of active α-$MnO_2$ material during the 1st discharge.

Table S3. Mass change of cathode materials in α-$MnO_2$ electrode.

| α-$MnO_2$ electrode | Mass of cathode materials (mg) |
|---|---|
| Before discharge | 5 |
| After the 1st discharge | 8.9 |
| After the 1st discharge with acetic acid treatment | 3.8 |

The electrodes were washed with deionized water and vacuum dried at 60 °C overnight to exclude any influence of surface-adsorbed water. After the 1st discharge, the mass increased significantly due to the formation of ZHS plates. After ZHS was removed by acetic acid treatment, the mass decreased compared with the fresh electrode.

ICP measurement was also performed to justify the dissolution of α-$MnO_2$. Electrolytic cell was assembled with an α-$MnO_2$ electrode as the cathode, a Zn disc as the anode, 2 M $ZnSO_4$ (20 mL) as the electrolyte. The α-$MnO_2$ electrode delivered a discharge capacity of 220 mAh $g^{-1}$ during the 1st cycle. After the 1st discharge, ICP result shows that the concentration of $Mn^{2+}$ in electrolyte is 25.42 ppm (equal to 1.13 mg dissolved α-$MnO_2$). The decreased mass of α-$MnO_2$ electrode and the high concentration of $Mn^{2+}$ in electrolyte after discharge provide compelling evidence for the dissolution of α-$MnO_2$.

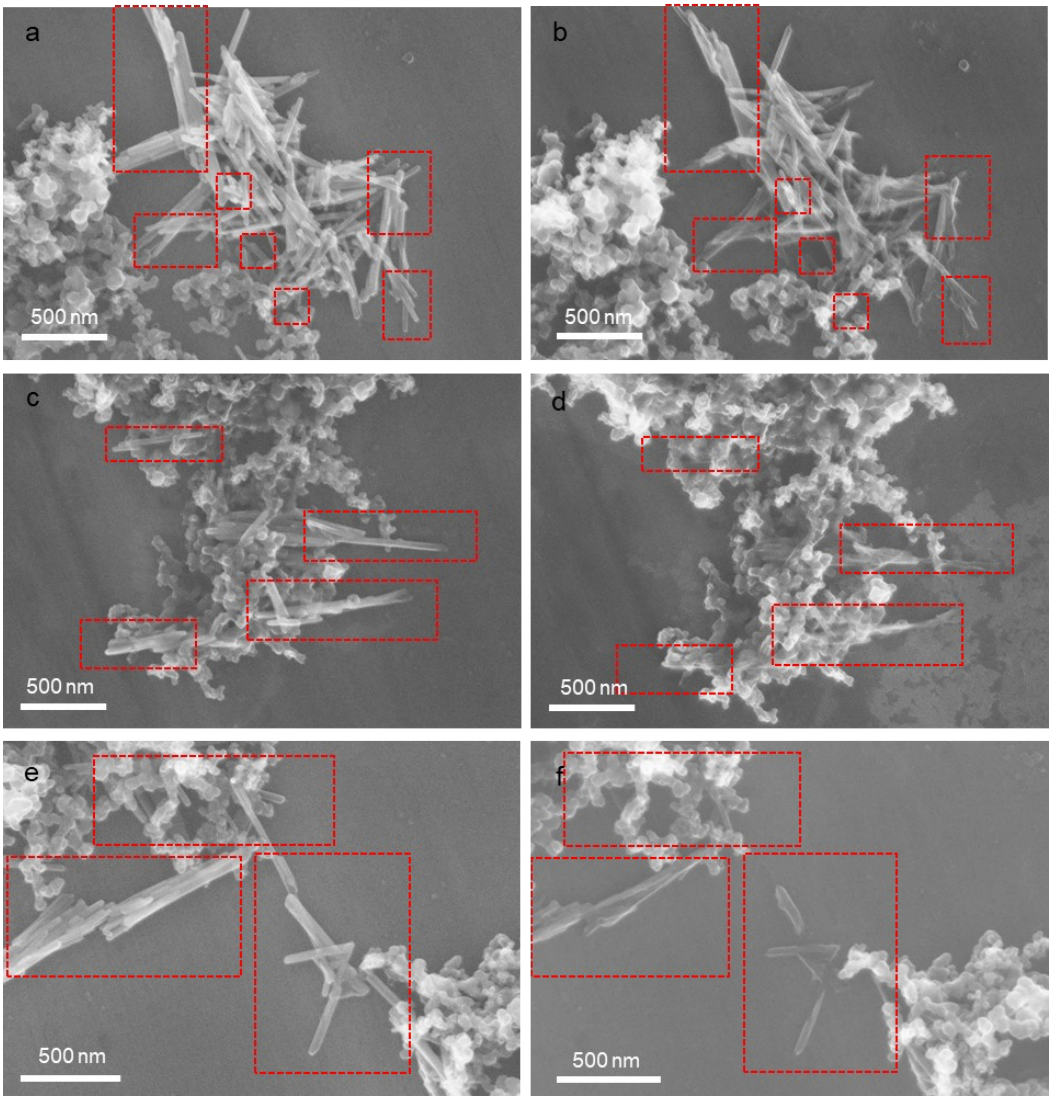


Fig. S6 SEM images of α-$MnO_2$ electrode in three different locations before and after the 1st discharge. (a,c,e) Before the 1st discharge, (b,d,f) After the 1st discharge.

The α-$MnO_2$ electrodes with trace cathode materials for *ex situ* SEM characterization were prepared as follows. Solution of cathode materials were prepared by mixing α-$MnO_2$ particles, conductive carbon black (Super P) and poly(1,1-difluoroethylene) with a weight ratio of 7:2:1 in N-methylpyrrolidone. The electrode was obtained by dripping the solution on stainless steel foil, and then through vacuum drying at 80 °C overnight.

Electrolytic cell was assembled with an α-$MnO_2$ electrode as the cathode, a Zn disc as the anode, 2 M $ZnSO_4$ as the electrolyte. After the 1st discharge, the α-$MnO_2$ electrodes were immersed in deionized water to remove the residual electrolyte. The red box signed in SEM images show that some α-$MnO_2$ nanorods shortened, thinned or even disappeared, indicating the loss of active α-$MnO_2$ during the 1st discharge.

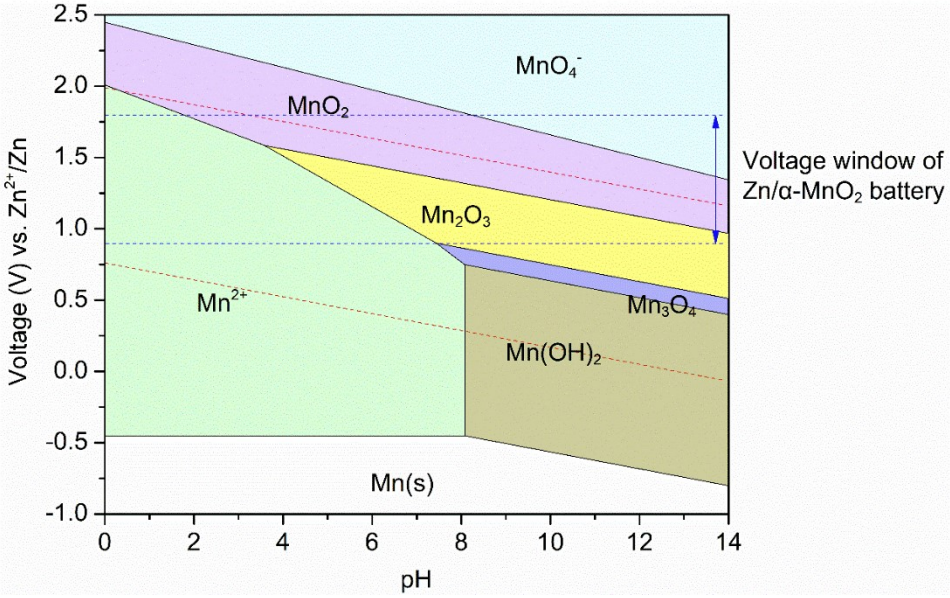


Fig. S7 *E*-pH diagram of Mn-$H_2O$ system with 0.1 M $Mn^{2+}$ as the equilibrium concentration calculated with HSC chemistry 6 software.

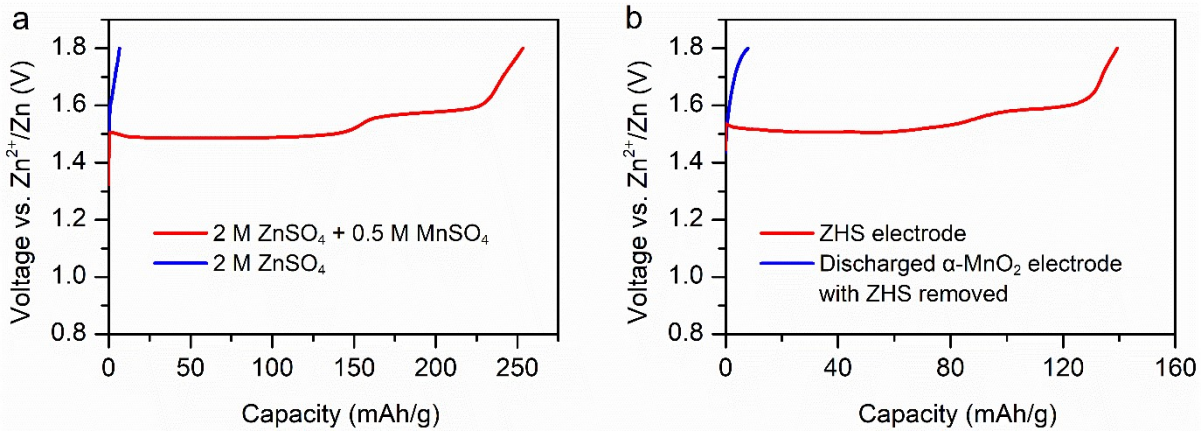


Fig. S8 Galvanostatic charge curves of discharged α-$MnO_2$ electrode, ZHS electrode and discharged α-$MnO_2$ electrode with ZHS removed. (a) Discharged α-$MnO_2$ electrode in 2 M $ZnSO_4$ with/without 0.5 M $MnSO_4$. (b) ZHS electrode and discharged α-$MnO_2$ electrode with ZHS removed in 2 M $ZnSO_4$ + 0.5 M $MnSO_4$.

Zn/α-$MnO_2$ batteries with electrolyte of 2 M $ZnSO_4$ were discharged to 0.9 V at 30 mA $g^{-1}$ and then disassembled. Discharged α-$MnO_2$ electrodes were washed with deionized water to remove the $Mn^{2+}$ in electrolyte dissolved from α-$MnO_2$ during discharge and then re-assembled with fresh electrolyte (2 M $ZnSO_4$ with/without 0.5 M $MnSO_4$) and Zn anode. The treated α-$MnO_2$ electrode delivered a limited charge capacity of 6.7 mAh $g^{-1}$ in 2 M $ZnSO_4$ electrolyte which is attributed to $H^+$ extraction from α-$MnO_2$. In contrast, higher charge capacity of 253.3 mAh $g^{-1}$ was obtained in electrolyte of 2 M $ZnSO_4$ + 0.5 M $MnSO_4$. To unveil the role of ZHS on deposition reaction, ZHS electrode and discharged α-$MnO_2$ electrodes with ZHS removed were charged in electrolyte of 2 M $ZnSO_4$ + 0.5 M $MnSO_4$. Discharged α-$MnO_2$ electrode with ZHS removed delivered a limited charge capacity of 7.9 mAh $g^{-1}$ which is attributed to $H^+$ extraction from α-$MnO_2$, whereas ZHS electrode delivered a charge capacity of 139.3 mAh $g^{-1}$. The corresponding SEM images show that the nanosheets of Zn-vernadite formed on discharged α-$MnO_2$ electrode in 2 M $ZnSO_4$ with 0.5 M $MnSO_4$ (Fig. S9c,d) and ZHS electrode in 2 M $ZnSO_4$ + 0.5 M $MnSO_4$ (Fig. S9g,h), whereas no Zn-vernadite was observed on discharged α-$MnO_2$ electrode in 2 M $ZnSO_4$ (Fig. S9a,b) and discharged α-$MnO_2$ electrode with ZHS removed in 2 M $ZnSO_4$ + 0.5 M $MnSO_4$ (Fig. S9e,f). These results demonstrate that both $Mn^{2+}$ and ZHS are essential in the formation of Zn-vernadite during charge.

The limited charge capacity of 6.7 mAh $g^{-1}$ for discharged α-$MnO_2$ electrodes in fresh 2 M $ZnSO_4$ and 7.9 mAh $g^{-1}$ for discharged α-$MnO_2$ electrode with ZHS removed in 2 M $ZnSO_4$ + 0.5 M $MnSO_4$ origin from $H^+$ extraction from α-$MnO_2$ indicate the limited $H^+$ intercalation/extraction in α-$MnO_2$, which can not explain the reduction of α-$MnO_2$ after discharge and the observable shift of α-$MnO_2$ peaks in *operando* XRD patterns. However, we

argue that the discharge/charge capacity origin from $H^+$ intercalation/extraction are higher than the observed limited charge capacity. Firstly, the continuous shift of α-$MnO_2$ peaks in *operando* XRD patterns during discharge indicate the $H^+$ intercalation reaction is active throughout the discharge process. Secondly, The observation that Zn-vernadite gradually dissolved/formed during discharge/charge process (Fig. 3) indicate the active dissolution/deposition reaction of Zn-vernadite throughout the discharge/charge process, which agree with previous report that the $Mn^{2+}$ concentration in electrolyte during discharge/charge continuously increase/decrease.[3] Thus, it is reasonable that $H^+$ intercalated into α-$MnO_2$ forming α-$H_xMnO_2$ then α-$H_xMnO_2$ dissolved. Consequently, less $H^+$ extracted from residual α-$MnO_2$ during charge compared to that intercalated into α-$MnO_2$ during discharge.

It has been reported that $Mn^{2+}$ was electro-oxidized to $MnO_2$ using a constant-voltage technique.[4-6] However, we need to point out that the electro-oxidation of $Mn^{2+}$ to $MnO_2$ is hardly to happen for the discharged $MnO_2$ electrode (ZHS removed) with 2 M $ZnSO_4$ + 0.5 M $MnSO_4$ electrolyte and barely deliver capacity (Fig. S8b) because of the galvanostatic condition.

Zn/carbon cloth batteries with 2 M $ZnSO_4$ + 0.5 M $MnSO_4$ electrolyte were assembled and galvanostatic charged to 1.8 V at the same current with the discharged $MnO_2$ electrode (ZHS removed). We found the voltage of Zn/carbon cloth batteries rapidly increased to 1.8 V and there are a relatively limited capacity of 0.0014 mAh was observed, which is equal to 0.5 mAh $g^{-1}$ for the discharged $MnO_2$ electrode (ZHS removed) in Fig. S8b. Consequently, the conclusion that the limited charge capacity for discharged α-$MnO_2$ electrode with ZHS removed in 2 M $ZnSO_4$ + 0.5 M $MnSO_4$ origin from $H^+$ extraction from α-$MnO_2$ is valid.

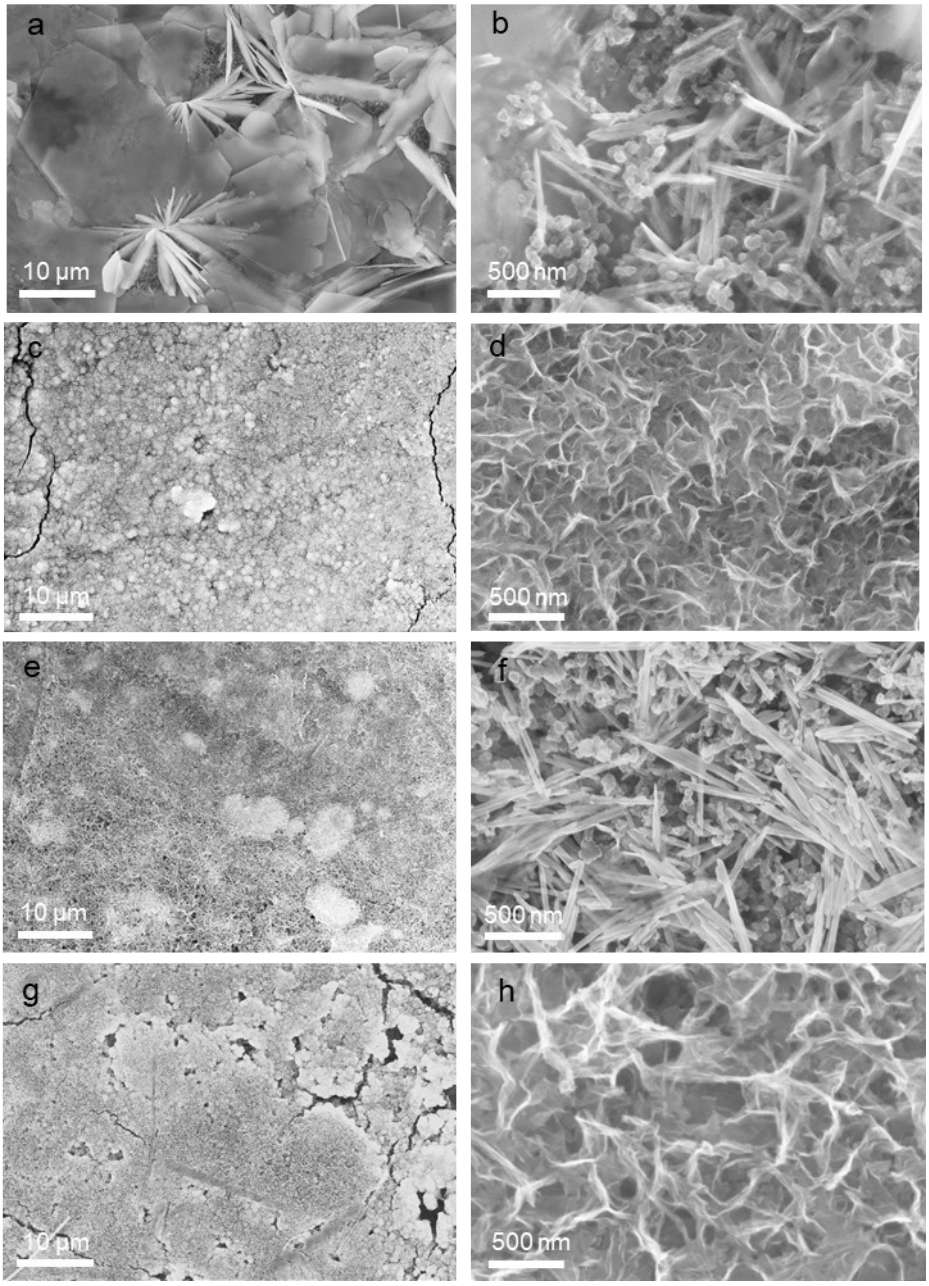


Fig. S9 SEM images of discharged α-$MnO_2$ electrode, ZHS electrode and discharged α-$MnO_2$ electrode with ZHS removed after the 1st charge. (a,b) Discharged α-$MnO_2$ electrode in 2 M $ZnSO_4$. (c,d) Discharged α-$MnO_2$ electrode in 2 M $ZnSO_4$ with 0.5 M $MnSO_4$. (e,f) Discharged α-$MnO_2$ electrode with ZHS removed in 2 M $ZnSO_4$ + 0.5 M $MnSO_4$. (g,h) ZHS electrode in 2 M $ZnSO_4$ + 0.5 M $MnSO_4$.

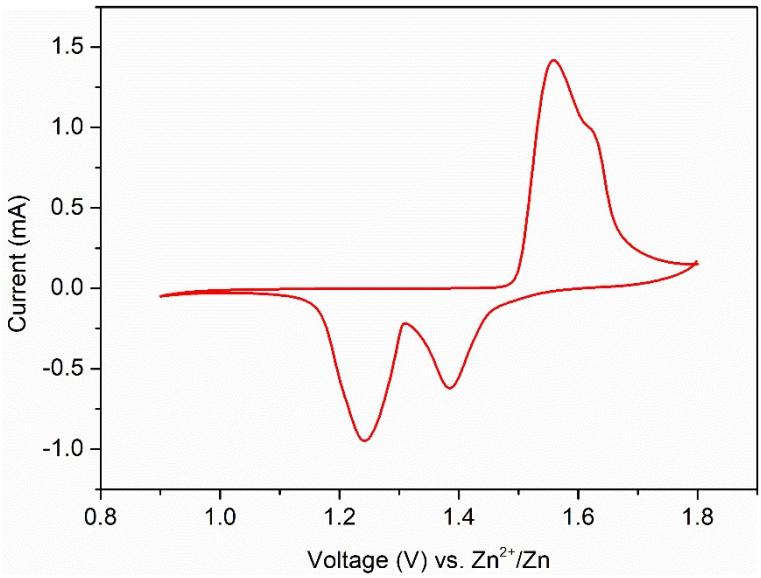


Fig. S10 CV curve of α-$MnO_2$ electrode (0.1 mV $s^{-1}$, the second cycle).

The voltage ranges of the reduction peaks at 1.38 V ($R_1$) and 1.24 V ($R_2$) are consistent with those of the plateaus I and II. Thus the electrochemical reactions occurred in plateaus I and II correspond to the two reduction peaks in CV curve. We revealed that the electrochemical reactions occurred at the two discharge plateaus are $H^+$ intercalation in α-$MnO_2$ and electrochemical dissolution of Zn-vernadite, respectively. The reason is as follows. The continuous shift of α-$MnO_2$ peaks in *operando* XRD patterns indicate the $H^+$ intercalation/extraction reaction is active throughout the discharge/charge process. SEM images show that Zn-vernadite gradually dissolved/formed during discharge/charge process, which agree with the observation previous reported that the $Mn^{2+}$ concentration in electrolyte during discharge/charge continuously increase/decrease indicating the active dissolution reaction of α-$MnO_2$ throughout the discharge/charge process. Consequently, both $H^+$ intercalation reaction and dissolution of α-$MnO_2$ are active in plateau I and II.

However, we note the $Mn^{2+}$ concentration in electrolyte during discharge/charge does not have a linear relationship with discharge/charge depth.[3] The $Mn^{2+}$ concentration increased significantly during plateau II. Thus, the capacity in plateau II mainly origins from the dissolution of vernadite. During plateau I, the discharge curve shows a smooth sloping, suggesting that a solid solution-like reaction[7] is dominant in plateau I. Consequently, we reason that $H^+$ intercalation in α-$MnO_2$ contributes more and the discharge capacity in plateau I mainly origins from $H^+$ intercalation reaction. Similarly, the charge capacities in plateau III and IV mainly origin from the deposition of Zn-vernadite and the $H^+$ extraction in α-$MnO_2$, respectively.

Consequently, two couples of redox peaks at 1.38 V ($R_1$)/1.62 V ($O_1$) and 1.24 V ($R_2$)/1.56 V ($O_2$) correspond to the $H^+$ intercalation/extraction in α-$MnO_2$ and electrochemical dissolution-deposition of Zn-vernadite respectively.

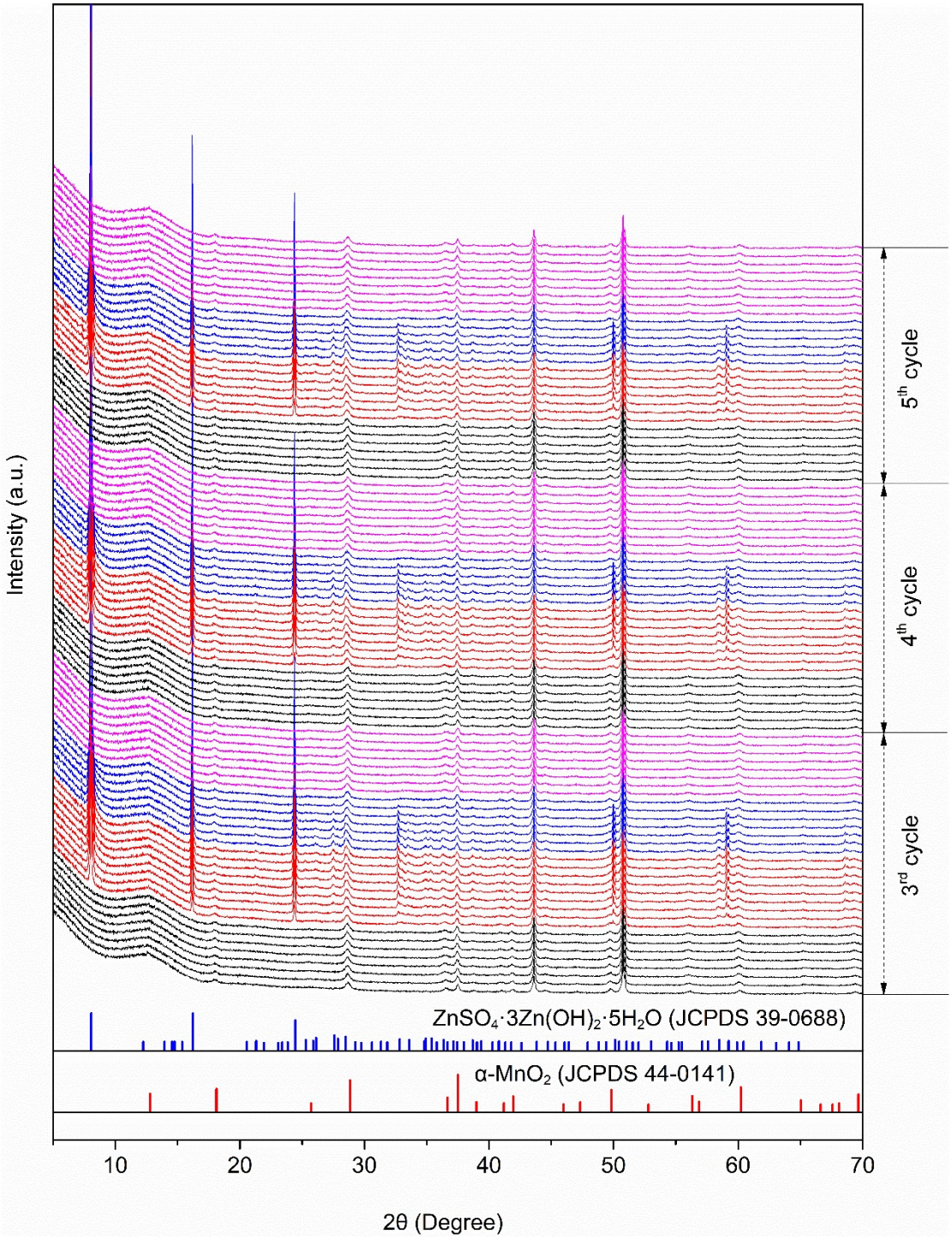


Fig. S11 *Operando* XRD patterns of α-$MnO_2$ electrode during the 3rd–5th cycles.

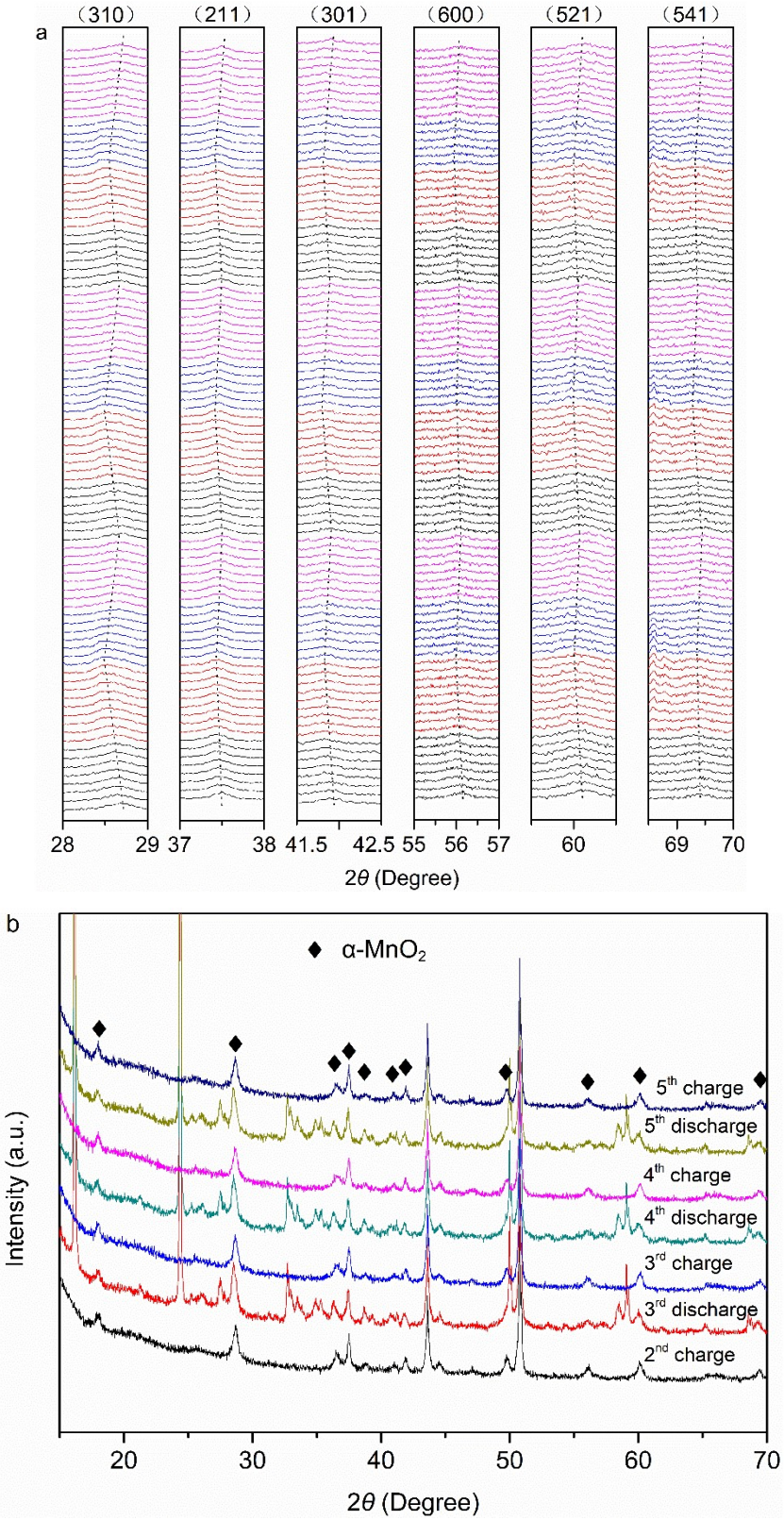


Fig. S12 (a) (310), (211), (301), (600), (521) and (541) peaks of α-$MnO_2$ in selected 2$\theta$ ranges. (b) XRD patterns collected at different charge-discharge states.

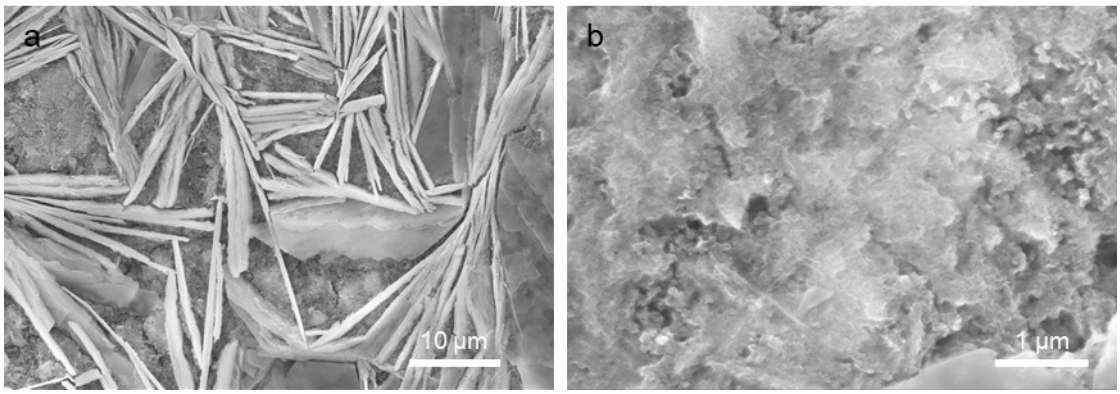


Fig. S13 SEM images of α-$MnO_2$ electrode after the 5$^{th}$ discharge. (a) Low magnification, (b) high magnification.

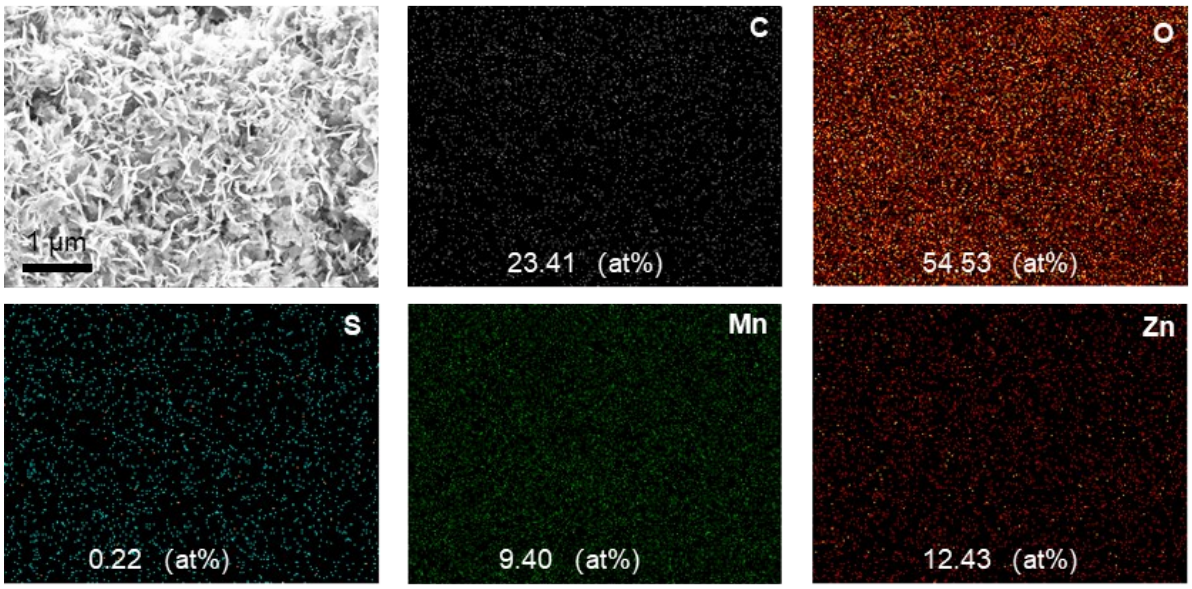


Fig. S14 SEM image and the corresponding EDS elemental mapping images of Zn-vernadite deposited on α-$MnO_2$ electrode after 200 cycles.

The trace amount of S is attributed to residual ZHS. Considering the atomic ratio of Zn:S=4:1 for ZHS, the atomic percentage of Zn from ZHS was excluded for calculation of the atomic ratio of Zn:Mn for Zn-vernadite.

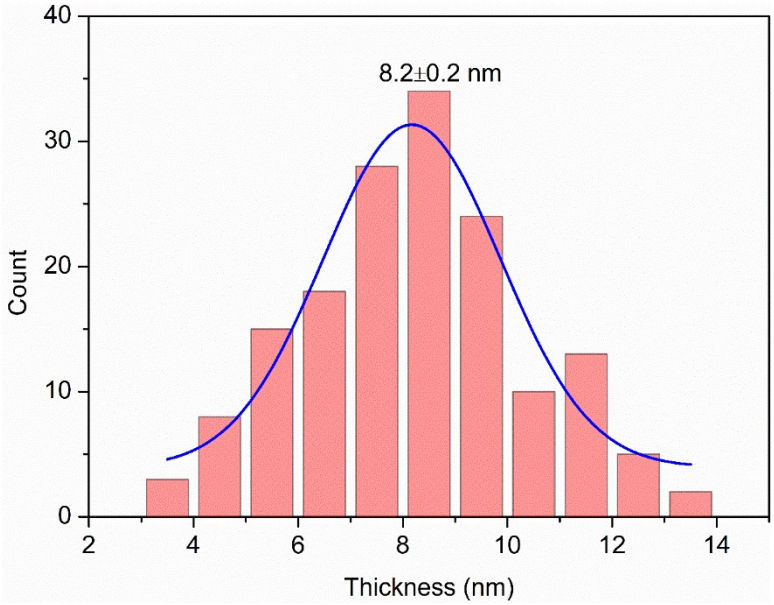


Fig. S15 Particle size statistics of Zn-vernadite nanoplates formed on α-$MnO_2$ electrode after 200 cycles.

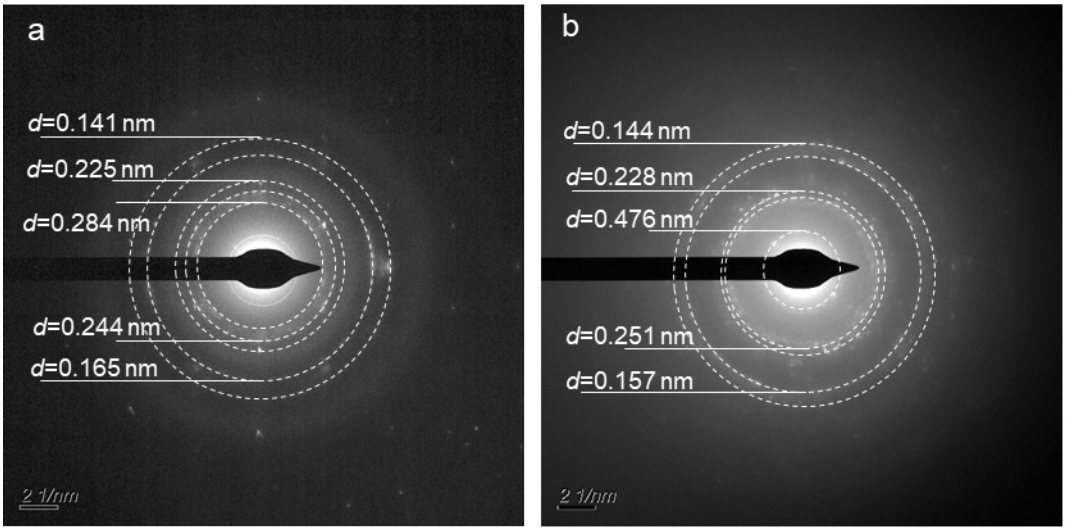


Fig. S16 SAED patterns of Zn-vernadite formed after the 1st cycle and 200 cycles with lattice spacings marked for corresponding planes (the precise plane indexes were not determined). (a) Zn-vernadite nanosheets formed after the 1st cycle. (b) Zn-vernadite nanoplates formed after 200 cycles.

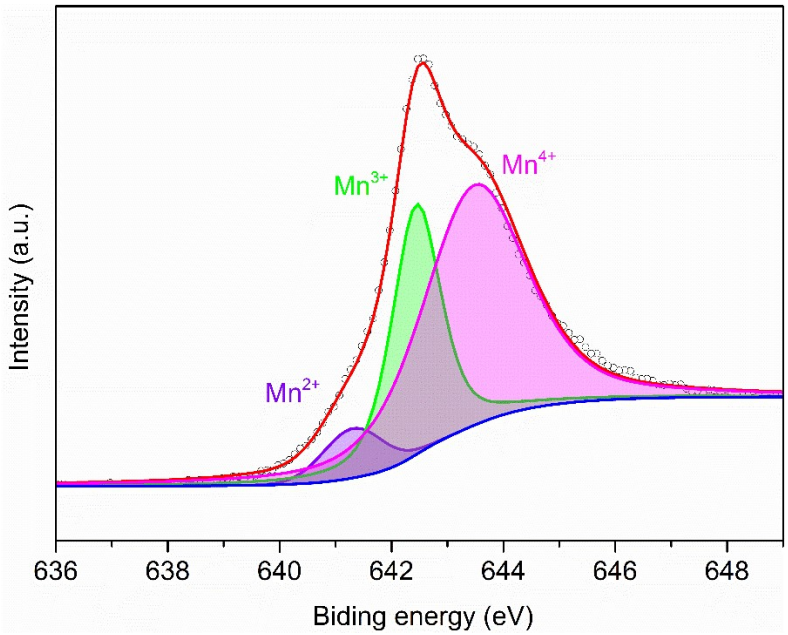


Fig. S17 Mn 2p spectra of Zn-vernadite formed on α-$MnO_2$ electrode after the 1st charge.

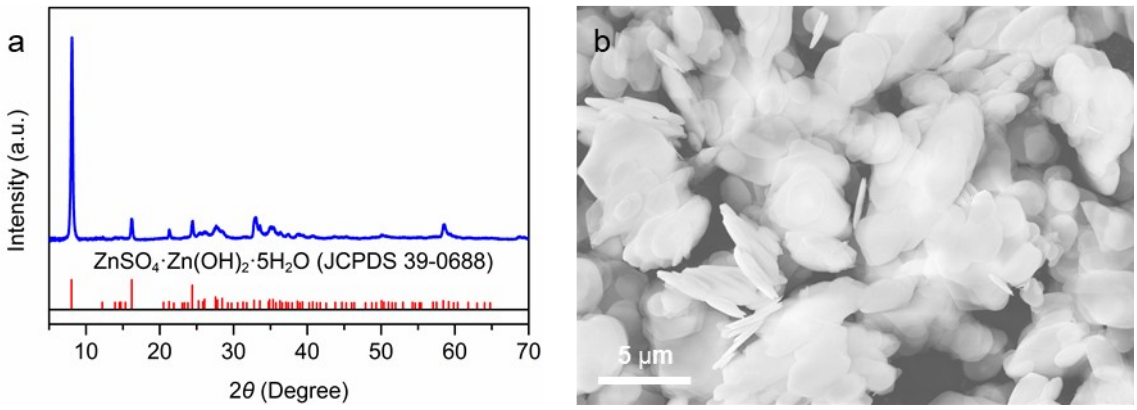


Fig. S18 XRD and SEM characterizations of ZHS. (a) XRD pattern. (b) SEM image.

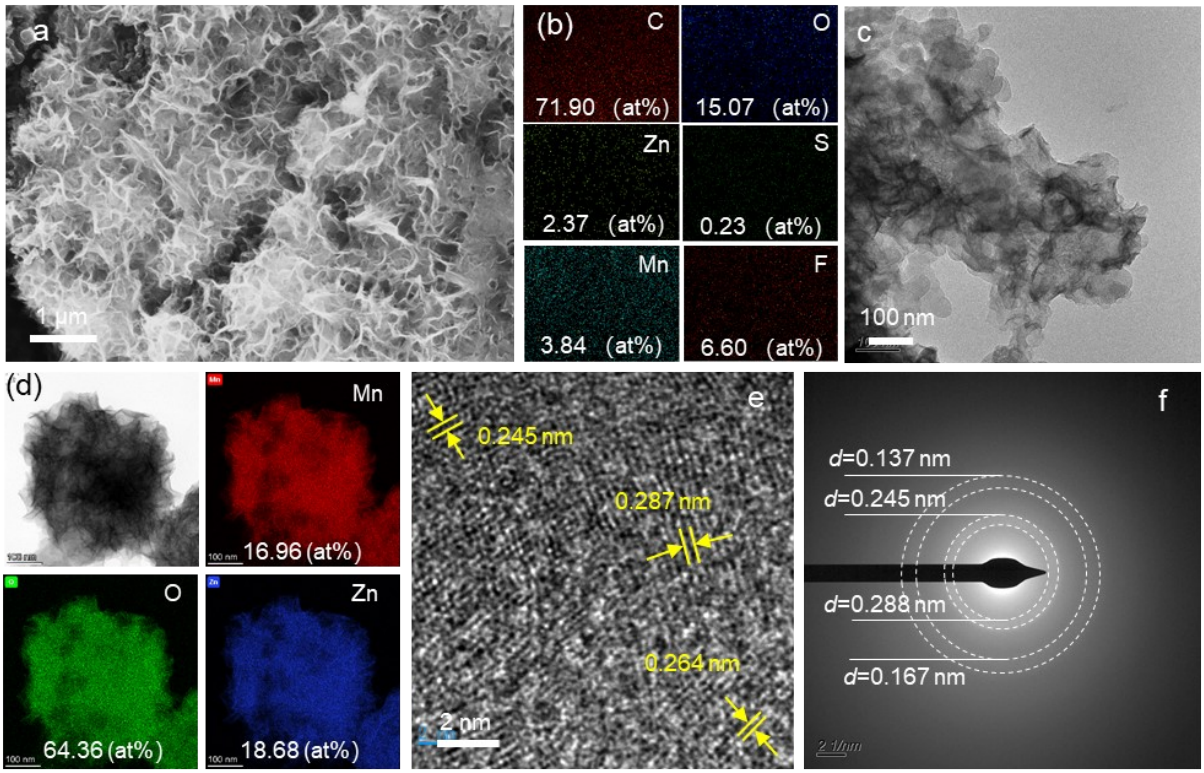


Fig. S19 SEM and TEM characterizations of Zn-vernadite nanosheets formed on ZHS electrode after the 1st charge. (a) SEM image. (b) SEM EDS elemental mapping images. (c) TEM image. (d) TEM EDS elemental mapping images. (e) HRTEM image. (f) SAED pattern.

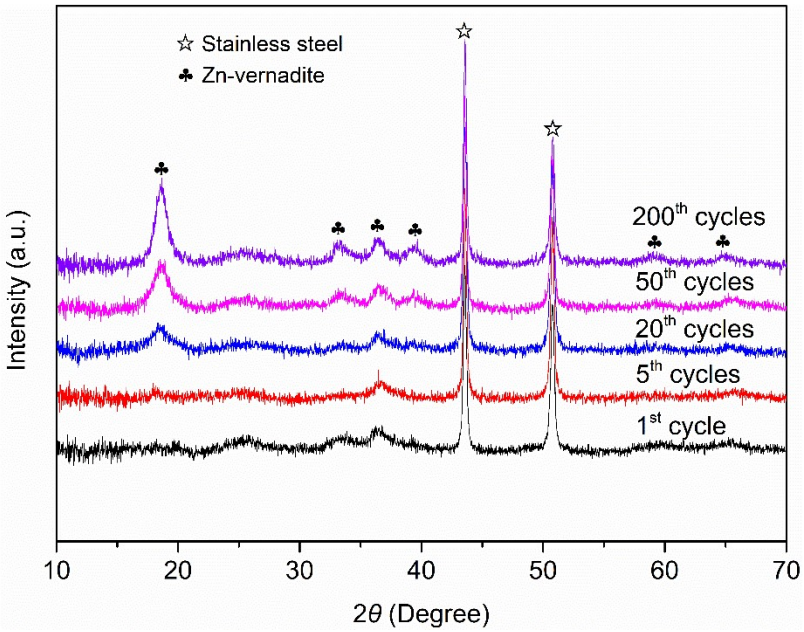


Fig. S20 *Ex situ* XRD patterns of ZHS electrode during long cycles (1-200 cycles) with the current density of 300 mA $g^{-1}$. The XRD pattern for the 1st cycle was obtained with step size of 0.02° and step time of 1 s, whereas other patterns were obtained with step size of 0.02° and step time of 0.5 s.

The peak at 18.63° was not observed in XRD pattern for Zn-vernadite monolayers formed after the 1st cycle. With increasing cycles, the peak intensity at 18.63° of Zn-vernadite gradually increased. Zn-vernadite formed at initial cycles and after long cycles is the same phase based on XRD and TEM results as shown in Fig. S19 and Fig. S21.

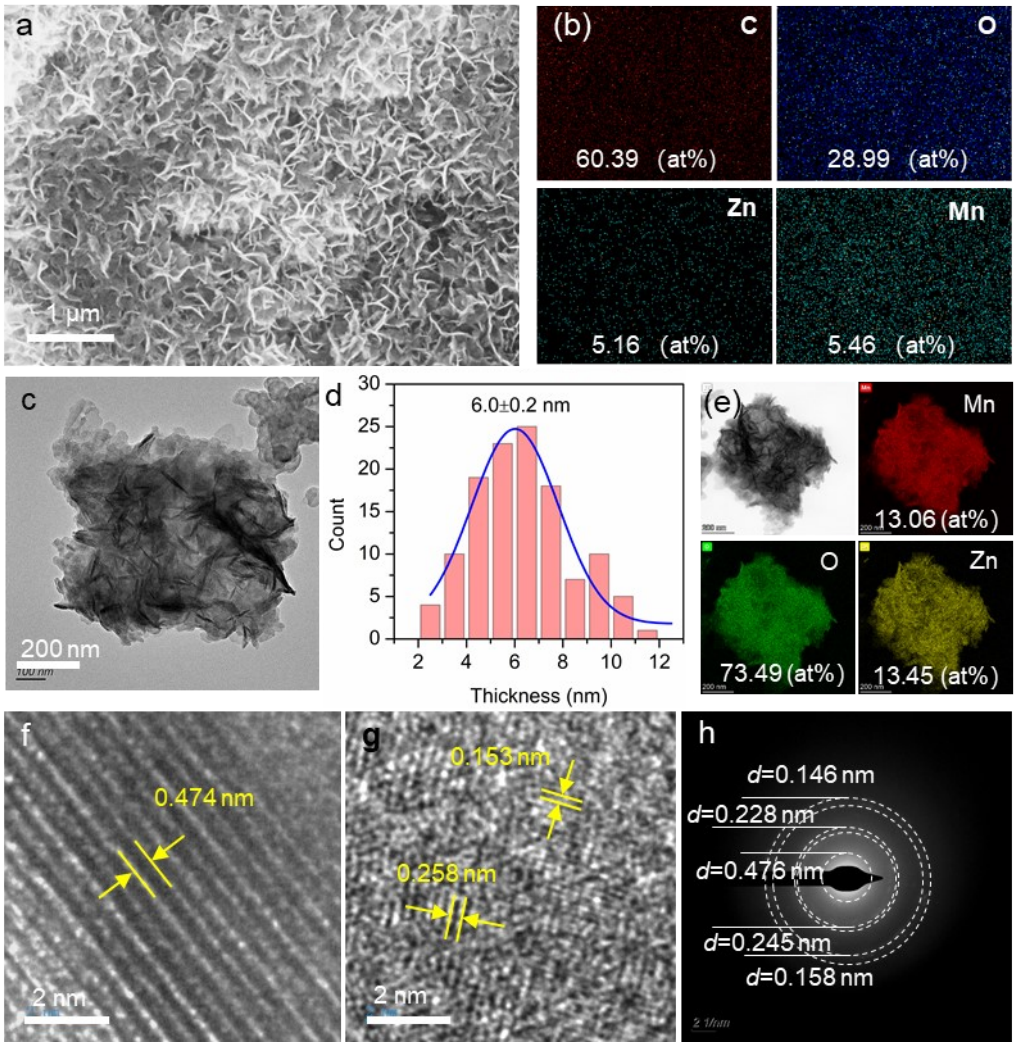


Fig. S21 SEM and TEM characterizations of Zn-vernadite nanoplates formed on ZHS electrode after 200 cycles. (a) SEM image. (b) SEM EDS elemental mapping images. (c) TEM image. (d) particle size statistics. (e) TEM EDS elemental mapping images. (f,g) HRTEM images. (h) SAED pattern.

SEM image shows the full coverage of thicker nanoplates. TEM image of multiple particle size statistics shows an average thickness of 6.0 ± 0.2 nm. SEM and TEM mapping images give the atomic ratio of Zn:Mn~1:1. Vernadite nanoplates formed after 200 cycles and vernadite nanosheets formed after the 1$^{st}$ cycle share identical intralayer structure and similar elemental composition as given in Fig. S19 and Fig. S21.

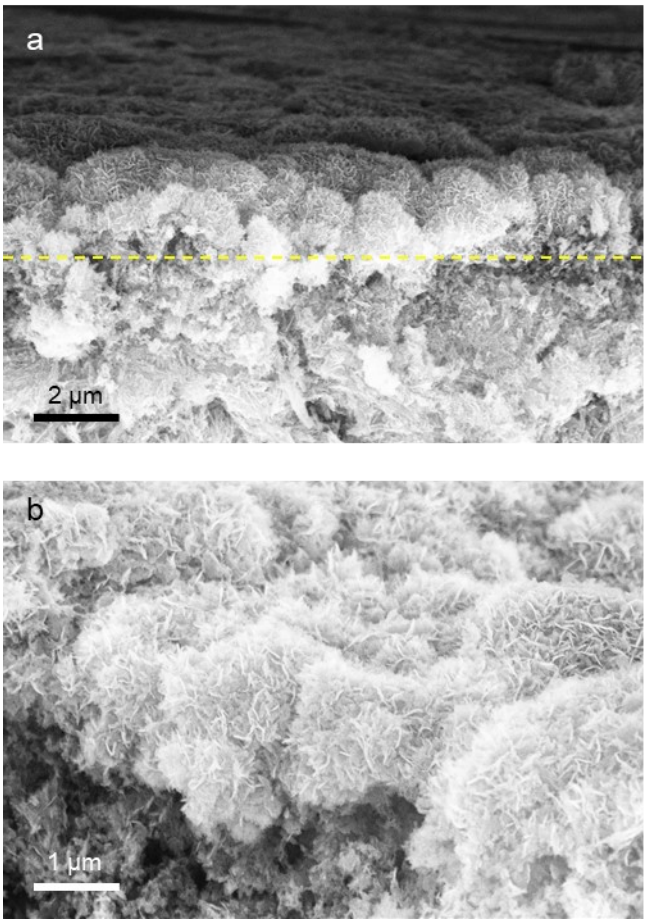


Fig. S22 SEM images of α-$MnO_2$ electrode after 200 cycles in cross-section view. (a) Low magnification, (b) high magnification.

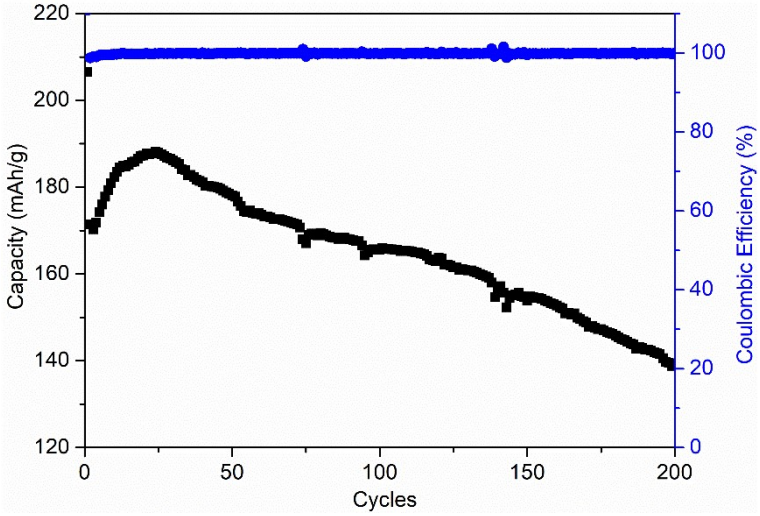


Fig. S23 Cycling performance of α-$MnO_2$ electrode at 300 mA $g^{-1}$

The capacity gradually increased in initial 25 cycles, which can be attributed to the activation of electrodes.[8, 9] Then, capacity faded during longer cycles: it decreased to 139 mAh $g^{-1}$ after 200 cycles. The capacity fading is attributed to the gradual dissolution of $MnO_2$ and the accumulation of vernadite. The α-$MnO_2$ electrode exhibits a stabilized Coulombic efficiency of ~100% except the 1st cycle. (Coulombic efficiency for the 1st cycle exceeds 100% because the deposition of vernadite is incomplete during the 1st charge.) In some cases, the irreversible reactions during cycles can be reflected in CE. However, it is inapplicable to explain the irreversible accumulation of vernadite. The reasons are as follows. Firstly, vernadite is electrochemically active. Both deposition and dissolution of vernadite during charge/discharge process contributed to capacity. Secondly, *ex situ* XRD results (Fig. 6a) show that α-$MnO_2$ peaks gradually weakened indicating the active dissolution reaction of α-$MnO_2$ throughout long cycles. Thirdly, the $H^+$ intercalation/extraction in α-$MnO_2$ is active before α-$MnO_2$ completely dissolved. Consequently, the CE for α-$MnO_2$ electrode actually reflect complex reactions including the dissolution of α-$MnO_2$, $H^+$ intercalation/extraction in α-$MnO_2$ and deposition/dissolution of vernadite rather than the single deposition/dissolution of vernadite. The stabilized CE during cycles may be attributed to the gradual dissolution of α-$MnO_2$ that compensated the decreased discharge capacity induced from the incomplete dissolution of accumulated vernadite.

The coulombic efficiency (%) was calculated based on charge and discharge capacities according to Eq. S1:

$$Coulombic\ efficiency = \frac{discharge\ capacity}{charge\ capacity} \times 100\% \quad (Eq.\ S1)$$

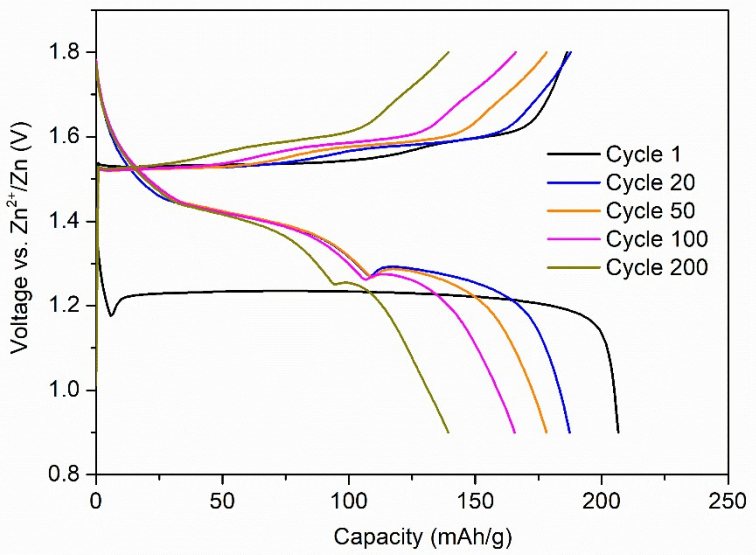


Fig. S24 GCD curves of α-$MnO_2$ electrode during long cycles (300 mA $g^{-1}$)

With increasing cycles the discharge capacity from plateau II gradually decreased whereas the discharge capacity from plateau I remained unchanged. The reasons are as follows.

The continuous shift of α-$MnO_2$ peaks in *operando* XRD patterns indicate the $H^+$ intercalation/extraction reaction is active throughout the discharge/charge process. SEM images show that Zn-vernadite gradually dissolved/formed during discharge/charge process, which agree with the observation reported previously that the $Mn^{2+}$ concentration in electrolyte during discharge/charge continuously increase/decrease indicating the active dissolution reaction of α-$MnO_2$ throughout the discharge/charge process. Consequently, both $H^+$ intercalation reaction and dissolution of α-$MnO_2$ are active in plateau I and II.

However, we note the $Mn^{2+}$ concentration in electrolyte during discharge/charge does not have a linear relationship with discharge/charge depth[3]. The $Mn^{2+}$ concentration increased significantly during plateau II. Thus, the capacity in plateau II mainly origins from the dissolution of vernadite. During plateau I, the discharge curve shows a smooth sloping, suggesting that a solid solution-like reaction[7] is dominant in plateau I. Considering that the $H^+$ intercalation in α-$MnO_2$ is a solid solution-like reaction, we reason that $H^+$ intercalation in α-$MnO_2$ is more active than the dissolution of α-$MnO_2$ and the discharge capacity from plateau I mainly origins from $H^+$ intercalation reaction.

With increasing cycles, α-$MnO_2$ continues to dissolve, Zn-vernadite nanoplates continuously deposit on the electrode. The dissolution of α-$MnO_2$ during long-term cycles is relatively slow because the signals of α-$MnO_2$ were not disappeared even after 200 cycles as shown in *ex situ* XRD. Thus, $H^+$ intercalation reaction still delivers capacity before α-$MnO_2$ completely dissolved. Besides, we suppose that the intercalation reaction also occurred in Zn-vernadite and delivers capacity which also contribute to maintain the discharge capacity from plateau I. Now we are working on the elucidation of the detailed electrochemical reaction

process of Zn-vernadite.

Accumulation of deposited thick Zn-vernadite nanoplates over the electrode can cause poor physical contact of Zn-vernadite with underlying conductive black and collector, leading to the incomplete dissolution of Zn-vernadite and reduced contribution of capacity from electrochemical dissolution of Zn-vernadite. Consequently, the discharge capacity from plateau II gradually decreased.

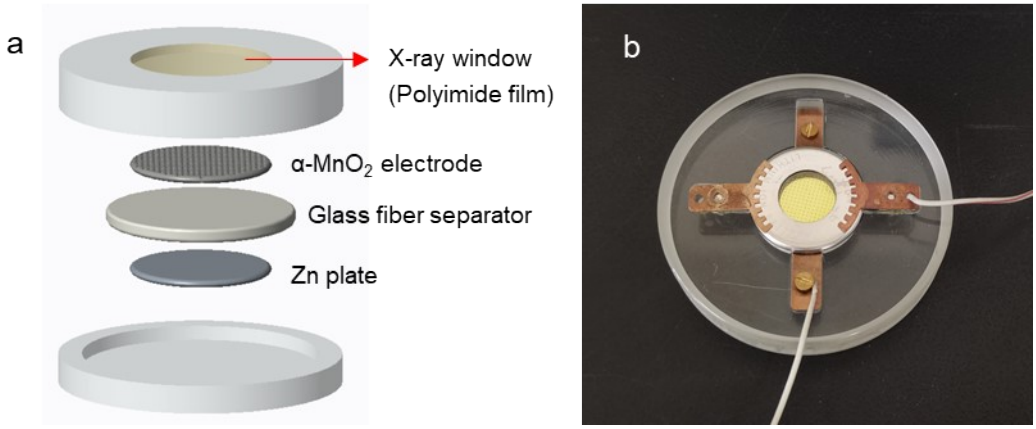


Fig. S25 (a) Schematic of the modified coin cell for *operando* XRD measurements. (b) Photo of the customized cell holder for *operando* XRD measurements.

**Supplementary Discussions**:

1. Contributions of $H^+$ intercalation and dissolution of α-$MnO_2$ to the formation of ZHS during discharge

XPS results (Figure. 4a) show the average oxidation state (AOS) of Mn decreased to 3.49 from 3.70 after the 1st discharge due to the $H^+$ intercalation. The decrease in AOS of 0.21 indicate that $H^+$ intercalation reaction consumed 0.0084 mmol $H^+$ and delivered a capacity of 65 mAh $g^{-1}$ (Eq. 1). According to the discharge capacity of 205 mAh $g^{-1}$ during the 1st cycle, the dissolution of α-$MnO_2$ delivered a capacity of 140 mAh $g^{-1}$ consumed 0.0366 mmol $H^+$ (Eq. 2). Consequently, both $H^+$ intercalation reaction and the dissolution of α-$MnO_2$ contribute to the formation of ZHS and the dissolution of α-$MnO_2$ contributes more than $H^+$ intercalation reaction. Now the discussions were added in this revision.

2. The different pH changes during the 1st discharge and following cycles

As shown in Fig. 2a and Fig. S24, the discharge curve of the 1st cycle is different with the following cycles. The plateau II contributed much larger capacity in the 1st discharge. We believe that the difference of discharge curves between the 1st cycle and the following cycles is attributed to the different pH changes during the 1st discharge and the following discharge process. The reason are as follows.

Firstly, we need to clarify that the discharge curve is relevant to the pH changes during discharge. The turning point between the two discharge plateaus formed due to the formation of ZHS. We found ZHS was precipitated out in 2 M $ZnSO_4$ solutions at a pH of ~5.4. As we discussed in the manuscript, both $H^+$ intercalation and dissolution of $MnO_2$ lead to the assumption of $H^+$ and result in the increase of pH. This indicate that the pH of electrolyte gradually increased during discharge (the original pH value of the electrolyte is ~4). Then ZHS formed when the local pH of the electrode surface increased to 5.4. The $c(OH^-)$ in electrolyte dropped rapidly after the nucleation of ZHS. The formation of ZHS maintained the stability of interfacial pH value. According to Nernst equation, the rapid decrease of $c(OH^-)$ in electrolyte caused by the formation of ZHS leads to the abnormal voltage increase during discharge. Thus the tuning point in discharge curves at ~1.3 V (Fig. 2a) caused by the abnormal voltage change represents the formation of ZHS. This statement can be verified by previous report.[10]

During the 1st cycle, the cells were discharged from open circuit potential (~1.4 V). The voltage drop rapidly to the turning point at ~1.3 V. During the following cycles, the cells were discharged from 1.8 V and the voltage gradually decreased to the turning point at ~1.3 V. This difference indicate that the local pH value decreased faster during the 1st discharge compared to others. *Operando* XRD results justified that ZHS formed later during the following cycles

compared with the 1st discharge. We have already discussed that the dissolution of $MnO_2$ is more active during plateau II than that in plateau I and the dissolution of $MnO_2$ contributes more for the assumption of $H^+$. Considering the different initial discharge voltage (~1.4 V for the 1st discharge and 1.8 V for the following cycles), the dissolution of $MnO_2$ is more active at the beginning of the 1st discharge and thus lead to the rapid assumption of $H^+$. Consequently, ZHS formed earlier during the 1st discharge and thus discharge curve shows larger capacity from plateau II.

References


1. C. Wang, Z. Pei, Q. Meng, C. Zhang, X. Sui, Z. Yuan, S. Wang and Y. Chen, *Angew. Chem. Int. Ed. Engl.*, 2021, **60**, 990-997.
2. H. Liang, Z. Cao, F. Ming, W. Zhang, D. H. Anjum, Y. Cui, L. Cavallo and H. N. Alshareef, *Nano Lett.*, 2019, **19**, 3199-3206.
3. D. Wu, L. M. Housel, S. J. Kim, N. Sadique, C. D. Quilty, L. Wu, R. Tappero, S. L. Nicholas, S. Ehrlich, Y. Zhu, A. C. Marschilok, E. S. Takeuchi, D. C. Bock and K. J. Takeuchi, *Energy Environ. Sci.*, 2020, **13**, 4322-4333.
4. D. Chao, W. Zhou, C. Ye, Q. Zhang, Y. Chen, L. Gu, K. Davey and S. Z. Qiao, *Angew. Chem. Int. Ed.*, 2019, **58**, 7823-7828.
5. X. Zeng, J. Liu, J. Mao, J. Hao, Z. Wang, S. Zhou, C. D. Ling and Z. Guo, *Adv. Energy Mater.*, 2020, **10**, 1904163.
6. G. Li, W. Chen, H. Zhang, Y. Gong, F. Shi, J. Wang, R. Zhang, G. Chen, Y. Jin, T. Wu, Z. Tang and Y. Cui, *Adv. Energy Mater.*, 2020, **10**, 1902085.
7. A. Van der Ven, J. Bhattacharya and A. A. Belak, *Acc. Chem. Res.*, 2013, **46**, 1216-1225.
8. B. Lin, X. Zhu, L. Fang, X. Liu, S. Li, T. Zhai, L. Xue, Q. Guo, J. Xu and H. Xia, *Adv. Mater.*, 2019, **31**, e1900060.
9. S.-D. Han, S. Kim, D. Li, V. Petkov, H. D. Yoo, P. J. Phillips, H. Wang, J. J. Kim, K. L. More, B. Key, R. F. Klie, J. Cabana, V. R. Stamenkovic, T. T. Fister, N. M. Markovic, A. K. Burrell, S. Tepavcevic and J. T. Vaughey, *Chem. Mater.*, 2017, **29**, 4874-4884.
10. Z. Liu, L. Li, L. Qin, S. Guo, G. Fang, Z. Luo and S. Liang, *Adv Mater*, 2022, **34**, e2204681.